



Contents lists available at ScienceDirect

Arabian Journal of Chemistry

journal homepage: www.ksu.edu.sa

Green fabrication, characterization and antimicrobial activities of AgO/Ag/carboxymethyl chitosan- graphene oxide films

Chen Li, Ke Wang, Fayong Li, Dong Xie*

Institute of Biological and Medical Engineering, Guangdong Academy of Sciences, Guangzhou 510316, China
 Guangdong Biomaterials Engineering Technology Research Center, Guangzhou 510316, China

ARTICLE INFO

Keywords:

UV-light-assisted reduction
 Silver
 Silver oxide
 Carboxymethyl chitosan
 Graphene oxide
 Antimicrobial

ABSTRACT

Antimicrobial AgO/Ag/carboxymethyl chitosan-graphene oxide (AgO/Ag/CGO) films were synthesized by UV-light-assisted reduction followed by ionic crosslinking method. The structure of the AgO/Ag/CGO films were explored by X-ray diffraction (XRD), field-emission scanning electron microscope (FE-SEM), Transmission electron microscopy (TEM), X-ray photoelectron spectroscopy (XPS), ultraviolet-visible spectroscopy (UV-vis), and Fourier-transform infrared (FTIR) analysis. We have also tested the cytotoxicity and cell viability of AgO/Ag/CGO³. The results of cytotoxicity of AgO/Ag/CGO³ on HepG2 cells suggests that the nanocomposite is not cytotoxic. Additionally, thermal stability, swelling ratio, antimicrobial activity of the AgO/Ag/CGO films were evaluated in detail, which revealed that the addition of GO improves the thermal stability and swelling ratio of AgO/Ag/CGO films. Of the three AgO/Ag/CGO films, the AgO/Ag/CGO³ exhibited better antimicrobial activity and higher inhibition rate against *E. coli* (89.2%) and *S. aureus* (93.4%). Therefore, the simple and green method is potential candidate for prepare of Ag-based antimicrobial film materials.

1. Introduction

Carboxymethyl chitosan (CMCS) as a novel amphoteric biopolymer, has been extensively applied in drug encapsulation, food, tissue engineering, cosmetic, antioxidant, and antibacterial fields owing to its properties of non-toxic, antimicrobial effect, biodegradable and biocompatible, required to meet many special conditions (Jie et al., 2022; Hao et al., 2022; Zhang et al., 2021; Shariatinia, 2018; Olanipekun et al., 2021). So, CMCS-base hybrid materials have obtained much attention in last few years (See Scheme 1).

Recently, the combination of mineral nanoparticles clay (Eddarai et al., 2022; Benucci et al., 2018; Biswas et al., 2021; Kausar et al., 2019; Lewandowska et al., 2014a; Lewandowska et al., 2014b), hydroxyapatite (Baskar et al., 2022; Ali et al., 2022; Furtos et al., 2013), graphene oxide (Azeman et al., 2022; Rostamian et al., 2022; Cao et al., 2022), metallic oxide and metallic such as zinc oxide (He et al., 2022; Wardana et al., 2022; Gasti et al., 2022) and Ag (Gao et al., 2022) with CMCS has been reported. Among them, GO has many advantages such as its large special surface area, hydrogen bonding, and simplicity of fabrication process, and has obtained a great interest in various fields. Additionally, GO can improve the mechanical property of CMCS-based hybrid

materials. In addition, Ag or AgO is another promising material to increase the antibacterial activity of CMCS, and has a wide application in clothing, pharmaceutical products, and medical devices due to its low toxicity and unique physical and chemical properties. There are several reports about CS-Ag, CS/Ag-WPU, GO/CMCS, and CMCS-AgO-Ag, nanocomposites, which have been applied in various areas including wound dressing (Zhou et al., 2021), food packaging (Cheng et al., 2021), water treatment (Su et al., 2021), and drug delivery system (Xu et al., 2020). Luo et al. (Luo et al., 2019) prepared graphene oxide/carboxymethyl chitosan aerogels via vacuum-assisted self-assembly and used for heavy metal adsorption. Huang et al. (Huang et al., 2017) synthesized the chitosan-nanosilver hybrids by in situ reduce method using glucose as the reducing agent. Pan et al. (Pan et al., 2020) prepared nanocomposite antibacterial films by in situ generation of silver nanoparticles and electrodeposition of carboxylate chitosan. Rasoulzadehzali et al. prepared the antibacterial chitosan/graphene oxide-Ag (CS-GO-Ag) bio-nanocomposite hydrogel beads for controlled release of doxorubicin (Rasoulzadehzali et al., 2018). However, there have been few reports on the preparation of antibacterial films by applying the antibacterial properties of silver ions (Ag²⁺) by a simple and green method.

To address this need, this work prepared the AgO/Ag/CGO

* Corresponding author.

E-mail address: xd0929@163.com (D. Xie).

nanocomposites films by a UV-light-assisted reduction and ionic cross-linking method. Then, the material was characterized by TEM, XPS, FE-SEM, XRD, and FTIR spectroscopy. The particle size distribution of the prepared Ag-NPs at different UV irradiation times were indicated by TEM. Moreover, we explored the thermal stability property and antimicrobial activity of the AgO/Ag/CGO nanocomposites films. We raise that the AgO/Ag/CGO nanocomposites films has an excellent antimicrobial and thermal stability property. As a consequence, it will be an efficient strategy to prepare novel nanocomposite antimicrobial materials.

2. Materials and methods

2.1. Materials and chemicals

Carboxymethyl chitosan (CMCS, 80 % of substitution degree), sodium hydroxide (NaOH, 96 %), Graphene oxide (GO) nanosheets were synthesized by the modified Hummers method, triphosphoric acid (99.8 %, TPP), silver nitrate (AgNO₃, 99.98 %), gelatin (C₁₃H₁₈O₂, ≥98 %), ethanol (C₂H₅OH, 99 %) and deionized water were all purchased from Macklin (Shanghai, China). All the reagents were of analytical grade.

2.2. Preparation of Ag nanoparticles

The Ag nanoparticles was synthesized by UV-light-assisted reduction. Simply, 0.4 g of gelatin was added to 20 mL deionized water in a flask under stirring; then the aqueous AgNO₃ was added dropwise to the clear gelatin solution; the mixed solution (Ag⁺/gel-sol) was placed into the UV reactor for UV irradiation at different times (1, 6, 12, 24 h) at room temperature to obtain the UV irradiated Ag nanoparticles.

2.3. Preparation of AgO/Ag/CGO films

The AgO/Ag/CGO films was synthesized by two steps. The as-prepared GO was dispersed in deionized water by stirring for 30 min and ultrasonicated for 30 min to obtain the dark brown solution. Firstly, 0.4 g CMCS was slowly dissolved in 20 mL water at 40 °C for 1 h to form a homogeneous solution and 20 mL of GO was added into the CMCS solution. After mixing, 1 mL of TPP solution (1 wt%) was added into above mixed solution and reacted for 2 h under continuous stirring to obtain the CGO solution. Secondly, the Ag/gel-sol (1, 6, 12, 24 h) was added into the CGO solution to react for 4 h to obtain the hydrogels and the resulting sol was cast onto glass plates to obtain the transparent films. The AgO/Ag/CGO films were recorded as AgO/Ag/CGO¹, AgO/Ag/CGO², AgO/Ag/CGO³, AgO/Ag/CGO⁴.

2.4. Characterizations of AgO/Ag/CGO films

Firstly, Ag/gel-sol samples synthesized under various UV irradiation times were characterized by UV-Vis spectroscopy from 300 to 700 nm. The morphology and microstructure of the CMCS-GO and AgO/Ag/CGO³, films samples were determined by FE-SEM (ZEISS MERLIN) and HRTEM (JEOL-2100F). X-ray diffraction patterns of the CMCS, CGO,

and AgO/Ag/CGO³ samples were recorded by XRD (X'Pert PRO Ultima IV) to analyze the phase structure. XPS analyses were investigated by a Thermo Scientific K-ALPHA + spectrometer with all the binding energies referenced to the adventitious carbon at 284.8 eV and the curve was fitted using XPS PEAK 4.1 software. FTIR spectra of CMCS, CGO, CMCS-Gellatin, and AgO/Ag/CGO samples were performed using a FTIR spectrophotometer (INVENIO-S). Raman spectrum of the samples was measured on a confocal Renishaw in Via Reflex Raman spectrometer.

2.5. Thermogravimetric analysis of AgO/Ag/CGO samples

The thermogravimetric analysis of the AgO/Ag/CGO film samples were determined via thermogravimetric analysis (TGA, TG209 F3). Simply, 5 ~ 10 mg of sample was placed in an alumina pans and putted into the crucible baskets at a heating rate of 20 °C /min range from 35 °C to 800 °C.

2.6. Water adsorbing ratio test

We detected the water adsorbing ratio of the film samples using a general gravimetric method. In brief, the film samples were putted into distilled water for 24 h at room temperature after weighed (M₀). After 24 h, the film samples were taken out and removed the moisture on the surface with filter paper before weighted again (M₁). The tests were carried out in triplicate and the average values were recorded. So the water adsorbing ratio AR (%) can be calculated using the following formula:

$$AR = (M_1 - M_0) / M_0 \times 100\% \quad (1)$$

Among them, M₀ is the initial weight of the sample, and M₁ is the weight of sample at 24 h.

2.7. Swelling ratio test

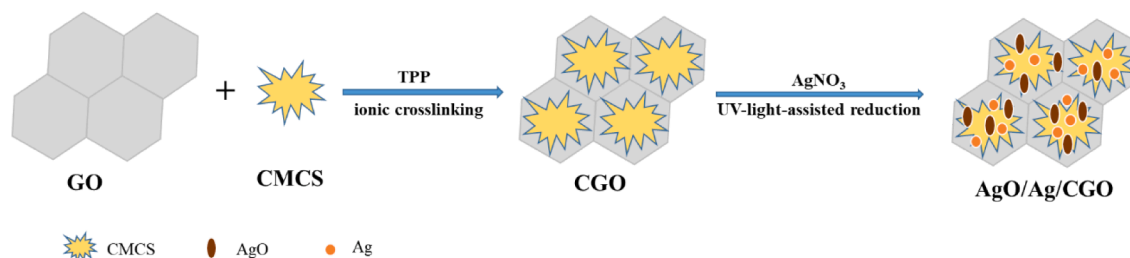
The swelling ratio of film samples was conducted in buffer solutions using a general gravimetric method. Briefly, the weighed samples were putted into the buffer solution separately in a shaking water bath at 37 °C. After 24 h, the swelling equilibrium was reached, and the samples were taken out and removed the droplets on their surface with paper towel. Then the samples were again weighed (W₁). The swelling ratio (SR) of samples was determined by the Eq. (2).

$$SR(\%) = (W_1 - W_0) / W_0 \times 100\% \quad (2)$$

Among them, W₀ is the initial weight of sample, and W₁ is the weight of sample at 24 h.

2.8. In vitro cytotoxicity analysis

To evaluate the cytotoxicity of nanocomposite, we tested the cytotoxicity of AgO/Ag/CGO³ on HepG2 cells via the MTT assay, and cell viability was determined after 24 h. The viability of the cultured cell was monitored using a cell MTT assay. Into a 96-well plate 100 μL HepG2 cell suspension of a density of 4000 cells/well was filled, and the culture



Scheme 1. Schematic illustration of the AgO/Ag/CGO films.

plate was put into an incubator at 37 °C with 5 % CO₂ for 24 h. Films samples was sterilized under UV light and thoroughly rinsed with phosphate buffer saline (pH 7.4) and added to the well for incubation for another 24 hours. Then, 20 μL MTT solution was added into each well and incubated for 4 h. Absorbance at 570 nm was measured with a Microplate Reader. The mean optical density (OD) of five wells was used to calculate the percentage of cell activity (CA) as:

$$CA = OD_t / OD_c \% \quad (3)$$

where OD_c and OD_t were the OD of the control sample and treated sample, respectively.

2.9. Determination of antibacterial activity of AgO/Ag/CGO films

The antimicrobial activity of AgO/Ag/CGO films against *E. coli* and *S. aureus* was investigated by qualitative and quantitative analysis, respectively. The antimicrobial activity of AgO/Ag/CGO films was qualitatively evaluated by disc diffusion assay, and the CGO film was used as negative control. Simply, *E. coli* as well as *S. aureus* was evenly spread on a nutrient agar plate medium at 37 °C respectively, and then the AgO/Ag/CGO films slices were placed on the medium. After incubation for 24 h, the bacterial growth was observed and the diameter of the zones of inhibition of these samples were measured. The tests were carried out in three times for each film. In addition, the inhibition rate of AgO/Ag/CGO films on *E. coli* and *S. aureus* have been determined by optical density (O.D) method. Simply, 0.5 g films were immersed in 30 mL of *E. coli* and *S. aureus* nutrient agar culture medium, and blank *E. coli* and *S. aureus* medium was used as control. These samples were incubated in thermostatic shakers for 12 h at a shaking rate of 50 rpm at 37 °C. Then the absorbance of the culture solution at 600 nm was measured with a UV-visible spectrophotometer. The inhibition ratio (IR) calculation formula is as follows:

$$IR = (A_{con} - A_t / A_{con} - A_0) \times 100\% \quad (4)$$

Here, A₀ is the absorbance before incubation of *E. coli*; A_t and A_{con} are the absorbance of *E. coli* in the film and the reference sample after incubation for t time.

2.10. In vitro silver-release study

The in vitro silver-release study was carried out by a previously described method, with slightly modification (Hosseini et al., 2013). The initial amount of silver and the amount of silver released from the AgO/Ag/CGO films were evaluated by inductively coupled plasma-optical emission spectrometry (ICP-AES, Iris Intrepid). 20 mg of AgO/Ag/CGO², AgO/Ag/CGO³, AgO/Ag/CGO⁴ were separately immersed in 20 mL of phosphate buffer (pH 7.4) and incubated at 37 °C under agitation. At various time intervals (4, 8, 12, 24, 48, and 72 h), samples were centrifuged and 1 mL of release medium were picked up for the analysis and an equal volume of fresh buffer was added into the device to maintain a constant volume. The concentration (ppm) of silver in the release medium was determined by ICP-AES analysis and then the cumulative release amount was calculated.

3. Result and discussion

3.1. Characterizations of Ag nanoparticles

In this work, we prepared the Ag nanoparticles by the UV irradiation method and the gelatin was used as a green stabilizer. The in-situ reduction of Ag⁺ involves radiolysis of aquatic solutions, and then are oxidized to form H⁺ and OH radicals (OH[•]) under UV irradiation (Equation (4)), and then the solvated electrons were produced. Then, metallic cations were reduced to the metallic atoms by the solvated electrons. At different UV irradiation times, we observed the color of the

Ag⁺/gel solutions and found that it gradually changed from colorless to yellow, then to brown, and finally dark brown, which suggesting the formation of Ag nanoparticles (Fig. 1a). To further ensure the formation of Ag nanoparticles, the UV-Vis spectroscopy was carried out and the result was shown in Fig. 1b. The appearance of absorption peak of the Ag⁺/gel solutions at about 420 nm indicated the formation of Ag nanoparticles, and the absorption spectrum peak increased with the increase of UV irradiation times (He et al., 2021; Niu et al., 2020; Nguyen et al., 2020). However, there is no absorption spectrum appearing of the sample prepared without UV irradiation, which indicating that UV irradiation played a crucial role for the synthesis of Ag nanoparticles.



3.2. Characterizations of AgO/Ag/CGO films

The morphology of freeze-dried AgO/Ag/CGO films was scrutinized by FE-SEM. In Fig. 2a, b, c, the cross-sectional micromorphologies of CGO shown an open porous network with a smooth surface. The pores distribute randomly but arrange regularly and most of the pore walls are interconnected. This porous structure and abundant hydrophilic polar groups not only facilitates water molecules to enter the network, but resulting in swelling, intercalation, and ion exchange properties. Compared with CGO, the morphology of AgO/Ag/CGO³ has not changed, but we cannot observe the silver and silver oxide particles on the surface of AgO/Ag/CGO³ sample due to the small particle size of silver and silver oxide. The XRD spectrum of the AgO/Ag/CGO³ and its reference samples was determined and the results were shown in Fig. 3a. CMCS showed a broad peak at 20.2° attributing to their anhydrous crystalline states. Compared with CMCS, the diffraction peaks of CGO and AgO/Ag/CGO³ shifted to lower diffraction angle owing to the enhanced interaction between CMCS and GO and the introduction of GO nanosheets destroying the anhydrous crystalline structure of CMCS (Xu et al., 2020). Additionally, the AgO/Ag/CGO³ sample exhibited three new diffraction peaks at 32°, 38° and 46°, which could be well attributed to the (111) plane of the AgO (JCPDS 43-1038) and (111), (200) planes of Ag (JCPDS 04-0783) (Lashin et al., 2021). Ag nanoparticles were prepared by the UV irradiation method, and the in-situ reduction of Ag⁺ involves radiolysis of aquatic solutions, and then are oxidized to form H⁺ and OH radicals (OH[•]) under UV irradiation (Equation (5)). AgO is formed by the reaction of Ag₂O with OH⁻ or the reaction of Ag with OH (Nwanyanya et al., 2013; Samsuddin et al., 2017). To further identify the valence state of silver and silver oxide, the X-ray photoelectron spectroscopy of the AgO/Ag/CGO³ was carried out. From the Fig. 3b, we can see that the Ag 3d XPS spectrum of AgO/Ag/CGO³ was fitted to two superimposed doublet. The peaks observed at 367.5 and 373.8 eV were corresponding to Ag⁰, and peaks at 367.2 eV and 373.2 eV are well attributed to Ag²⁺. These results are consistent with that of the XRD.

The FT-IR spectra of CMCS, CGO, AgO/Ag/CGO¹, AgO/Ag/CGO², AgO/Ag/CGO³, AgO/Ag/CGO⁴ were investigated to further confirm the formation mechanisms of the AgO/Ag/CGO hydrides. These results were shown in Fig. 4 and Fig.S1. In the characteristic peaks of CMCS, the characteristic peaks at 3305 cm⁻¹ and at 1576 cm⁻¹ attributing to the overlapping stretching vibrations of -NH and -OH and the -NH₂ deformation vibration and -COO- asymmetric stretching vibration overlapping, which shift to a lower frequency comparing to the spectra of CGO, suggesting the intermolecular hydrogen bonds between GO and CMCS (Azeman et al., 2022). The peak at 1079 cm⁻¹ is ascribed to the C-O stretching vibration of the secondary hydroxyl groups. Compare with CGO, it shifted to a lower frequency in AgO/Ag/CGO¹, AgO/Ag/CGO², AgO/Ag/CGO³, AgO/Ag/CGO⁴. This is may be attributed to the attachment of Ag or AgO. Additionally, a peak at around 1420 cm⁻¹ was attributed to the symmetrical stretching vibrations of the carboxyl groups, and the peak shifted to lower frequencies, which suggested that the -COOH groups may also contribute to silver immobilization.

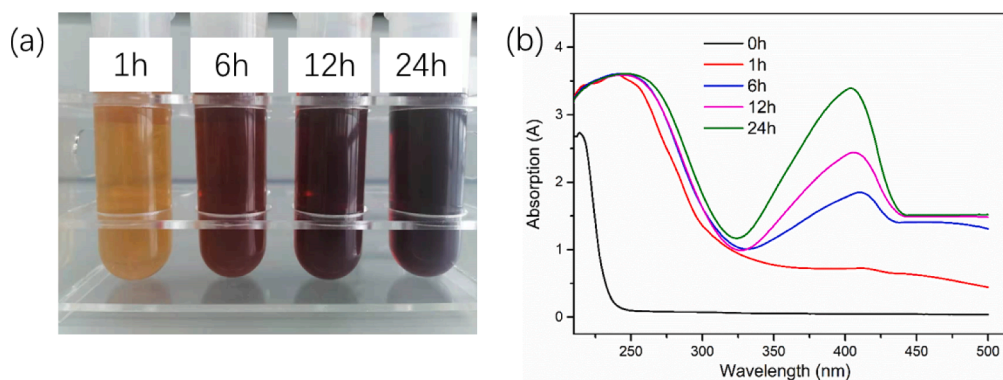


Fig. 1. Photograph (a) and UV-Vis spectra (b) of synthesized Ag-NPs in gelatin solution at different UV irradiation times.

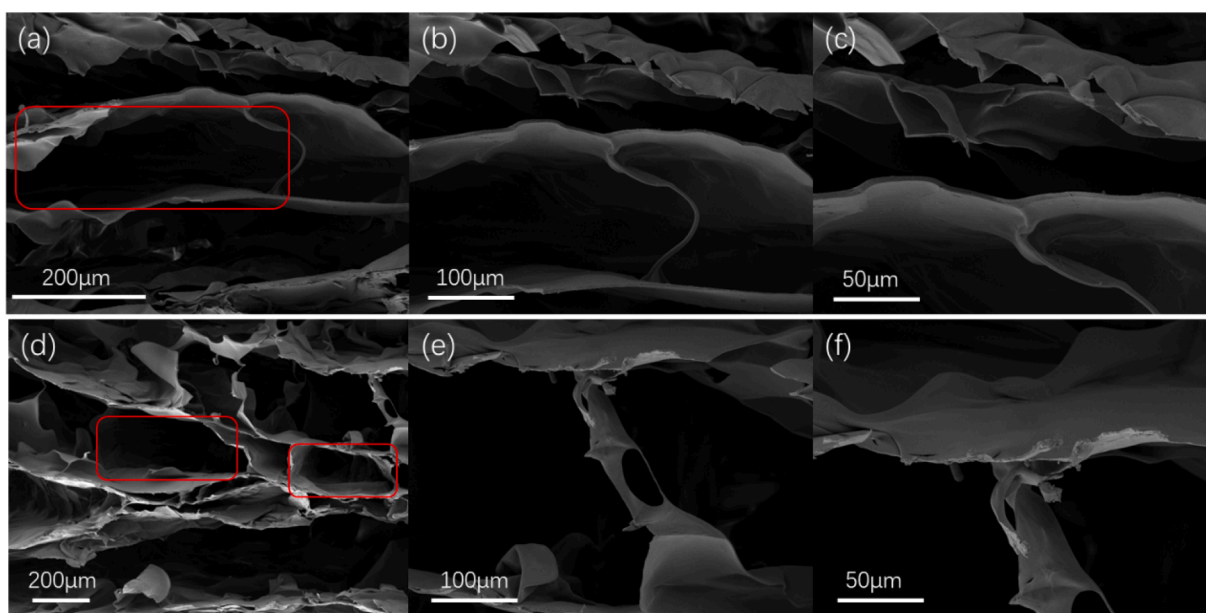


Fig. 2. FE-SEM images of (a, b, c) CGO and (d, e, f) AgO/Ag/CGO³ hydrogel samples.

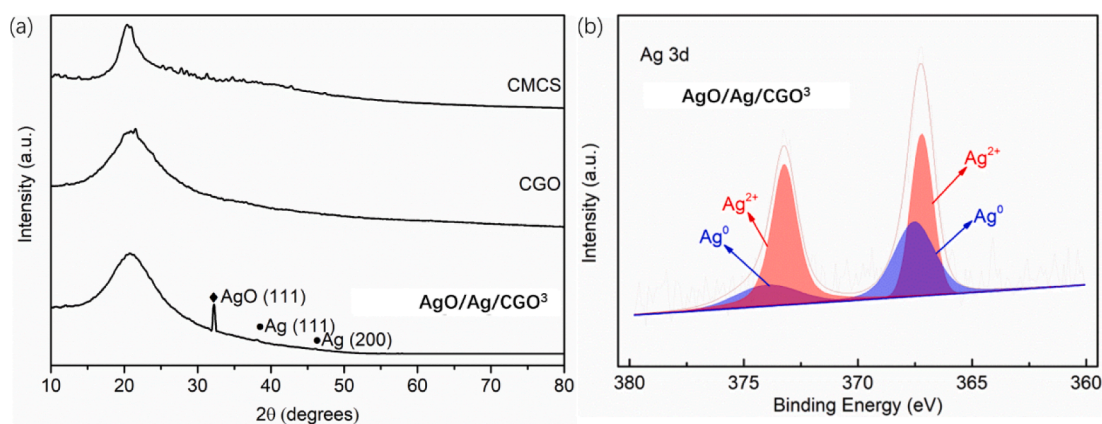


Fig. 3. The XRD patterns of CMCS, CGO and AgO/Ag/CGO³ (a); XPS patterns of Ag 3d of AgO/Ag/CGO³ sample (b).

To further determine the chemical composition, the chemical states of the GO, CMCS, CGO and AgO/Ag/CGO³ were investigated with XPS method. The C1s spectrum of CMCS-GO and AgO/Ag/CGO³ exhibits the same peaks with GO and CMCS at 284.1, 285.2, 286.6 and 287.3 eV, respectively (Fig. 5a, b, c, d). From Fig. 5e, N 1s spectrum of CMCS

exhibited three peaks at 399.1 eV, 398.5 eV, and 401.3 eV, which attributed to pyrrolic/pyridone (N-5), pyridinic (N-6), and quaternary nitrogen (N-Q), respectively. Similar to CMCS, the CGO and AgO/Ag/CGO³ also presents three peaks attributing to N-5, N-6, and N-Q, respectively (Fig. 4f, g). By the interacting between CMCS and GO, the

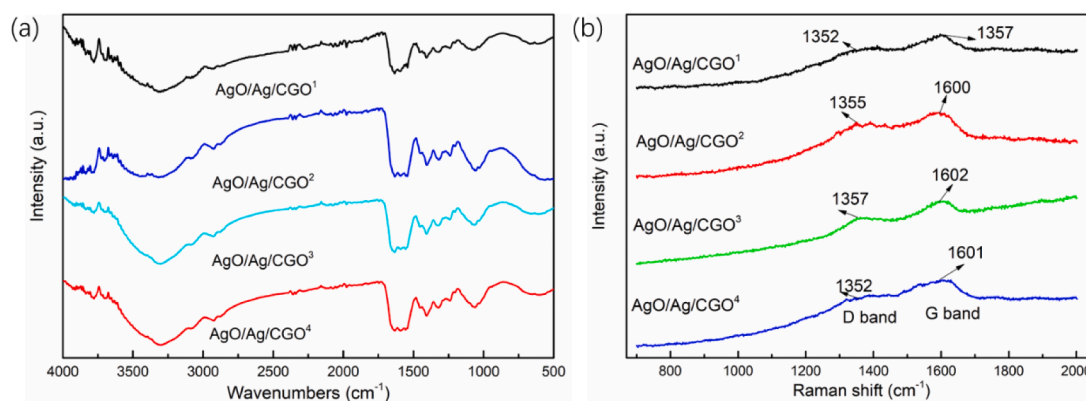


Fig. 4. FTIR spectra (a) and Raman spectra (b) of AgO/Ag/CGO¹, AgO/Ag/CGO², AgO/Ag/CGO³ and AgO/Ag/CGO⁴.

nitrogen content of N-5 decreases while the nitrogen content of N-6 and N-Q increases, suggesting that the N atoms of N-5 convert to N-6 and N-Q (Xu et al., 2020). Therefore, we can conclude that the CMCS is successfully assembled on the GO nanosheets by the hydrogen-bonding interaction. This result can be further confirmed by Raman spectra. From Fig. 4b, all samples exhibited two characteristic peaks at about 1355 cm⁻¹ (D band) and 1606 cm⁻¹ (G band), which are the two characteristic peaks of GO.

The TEM images show that Ag nanoparticles formed by reduction of Ag⁺ ions using the UV irradiation, and the corresponding particle size distribution of the Ag nanoparticles are shown in Fig. 6. From TEM image, we can see that spherical Ag nanoparticles were distributed homogeneously in the CMCS-GO network. Particle size and size distribution of the Ag nanoparticles in AgO/Ag/CGO¹, AgO/Ag/CGO², AgO/Ag/CGO³, AgO/Ag/CGO⁴ were measured and the Ag nanoparticles in AgO/Ag/CGO³ exhibited the narrowest size distribution (in the range of 4–5 nm) and the smallest mean diameter (4.72 ± 1.31 nm). This may be because of long time exposure of UV light results in the change of arrangement around the nanoparticle surface. However, AgO/Ag/CGO⁴ has a higher mean diameter than AgO/Ag/CGO³. This result may be attribute to the gelatin degradation under the long-term UV-irradiation source, which result in Ag nanoparticles could not enveloped in the gelatin framework agglomerate into larger particles. In Fig. 7, the HRTEM image and SAED pattern of AgO/Ag/CGO³ samples further demonstrated that Ag nanoparticles were crystalline in samples. The lattice spacings were identified to be 0.234 nm, which was indexed to the d-spacing of the Ag (111) plane (JCPDS 04-0783) (Huang et al., 2017; Duan et al., 2020; Biao et al., 2017). The SAED pattern showed periodic diffraction rings, which indicated that the Ag nanoparticles were polycrystalline.

3.3. Thermogravimetric analysis of AgO/Ag/CGO samples

The thermal properties of the AgO/Ag/CGO¹, AgO/Ag/CGO², AgO/Ag/CGO³, AgO/Ag/CGO⁴, were determined by TGA, as shown in Fig. 8a. We can observed that, in the temperature range of 35–500 °C, the weight loss of all samples could be divided into three stages. In the first stage, the all samples exhibited a weight loss from 35 °C to 120 °C, which attributing to the removal of physical adsorption and bound water. In the second stage, it exhibited a rapid weight loss from 120 °C to 250 °C, corresponding to the decomposition of functional groups on the polymer chain and the degree of reduction of each sample are difference. Notably, the decomposition temperature of the AgO/Ag/CGO¹, AgO/Ag/CGO², AgO/Ag/CGO³, AgO/Ag/CGO⁴ all samples was occurred at approximate 250 ~ 330 °C and lose their weight slowly. In addition, we can observed that the AgO/Ag/CGO² exhibited the biggest starting decomposition temperature, which suggest that the AgO/Ag/CGO² exhibited a higher better thermal stability than the other samples. This is

may be due to the gelatin degradation under the 12 h or 24 h UV-irradiation source, which destroy the network structure of the compound resulting in the decrease of thermal stability. In addition, Ag₂O first formed and it is not stability when the short UV-irradiation source. So the AgO/Ag/CGO² has a lower thermal stability than AgO/Ag/CGO¹.

3.4. Water adsorbing ratio and swelling ratio test

The water adsorbing ratio of the AgO/Ag/CGO¹, AgO/Ag/CGO², AgO/Ag/CGO³, AgO/Ag/CGO⁴ was tested, as shown in Fig. 8b. We can observed that the four samples exhibited high water absorption ratio in H₂O and swelling ratio in pH = 7.4 PBS. This is because of the existence of GO nanosheets creates more free spaces and higher porosity in the CMCS polymeric matrix. In addition, the interactions between GO and CMCS macromolecules also can enhance the water adsorbing ratio. Notably, the water absorption ratio and swelling ratio decreased with the increasing of the UV irradiation times, which resulted in the decrease of the amount of Ag⁺ ions. But the amount of Ag and AgO nanoparticles increased. This is due to the dispersion of Ag⁺ ions inside the polymer-networks, which can cause repulsion of networks and ultimately result in an improved swelling behavior of the system. So the water absorption ratio and swelling ratio decreased with the decreasing of the amount Ag⁺ ions (Gils et al., 2010). In addition, the amount of Ag and AgO nanoparticles increases with the increasing of the UV irradiation times, which indicated a more cross-linking point in the polymer-network, which prevent the aqueous medium from entering the polymer-network. So the water absorption ratio and swelling ratio decreased with the increasing of UV irradiation times (Xu et al., 2020).

3.5. Antimicrobial activities and cytotoxicity of AgO/Ag/CGO films

The antibacterial activity of the AgO/Ag/CGO films was studied the inhibition rings and inhibition rate against *E. coli* and *S. aureus*. The inhibition rings of the bacteria colonies on AgO/Ag/CGO², AgO/Ag/CGO³ and AgO/Ag/CGO⁴ films were presented in Fig. 9(a and b), and their diameters were 4.2 ± 0.1 mm, 5.2 ± 0.1 mm and 4.8 ± 0.2 mm against *E. coli* and 4.7 ± 0.2 mm, 5.4 ± 0.1 mm and 4.9 ± 0.2 mm against *S. aureus*, respectively. We can observe that the AgO/Ag/CGO², AgO/Ag/CGO³ and AgO/Ag/CGO⁴ films all exhibited excellent antimicrobial activities, which attributed to the presence of AgO/Ag in the films. Compared to AgO/Ag/CGO² and AgO/Ag/CGO⁴ films, the AgO/Ag/CGO³ film showed better antimicrobial activities. This is because of the narrowest size distribution (in the range of 4–5 nm) and the smallest mean diameter (4.72 ± 1.31 nm) of AgO/Ag/CGO³ film. In addition, the AgO/Ag/CGO³ showed stable and continuous silver release with no obvious initial burst. What is more, the AgO/Ag/CGO³ film showed a higher cumulative release of silver (Fig. 10). Therefore, the presence of AgO/Ag enhanced antimicrobial ability of CMCS-based nanocomposite

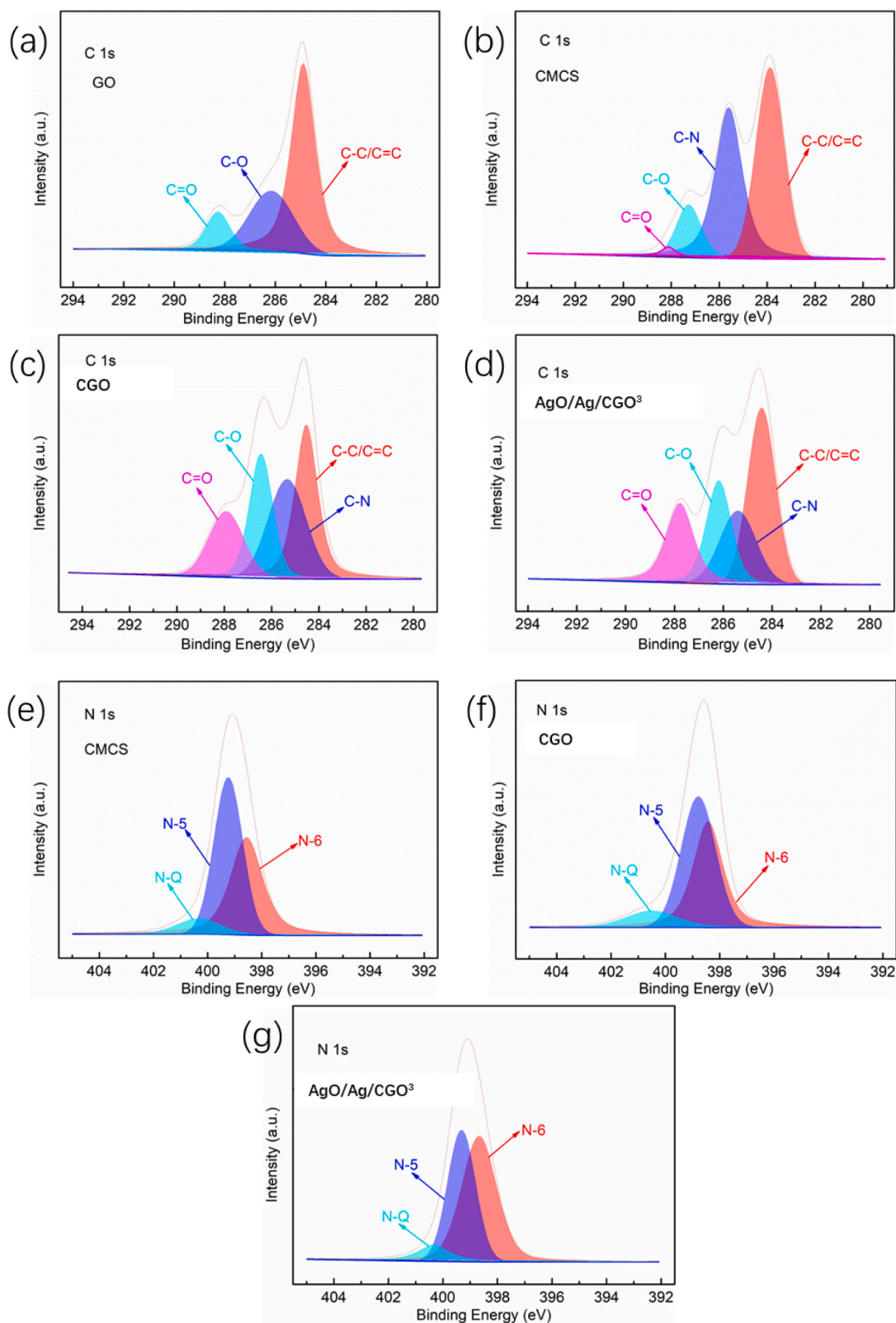


Fig. 5. XPS patterns of the surveys of GO, CMCS, CGO and AgO/Ag/CGO³. C1s of GO, CMC, CMCS-GO and AgO/Ag/CGO³ (a–d); N1s of CMCS, CGO and AgO/Ag/CGO³ (e–g).

significantly. In addition, the bacteriostatic ability of the AgO/Ag/CGO films is determined by the inhibition rate. From Fig. 9(c and d), we can find that the inhibition rate of AgO/Ag/CGO³ on *E. coli* (89.2 %) and *S. aureus* (93.4 %) is higher than other samples. These results are consistent with that of bacteriostatic zone test. The robust antimicrobial

activity of the film could additionally reduce the soft rotting of fresh produce and strengthen the safety of consumption. This would reduce microorganism spoilage which devastates fresh fruit and vegetables after harvest and might even reduce foodborne illness outbreaks when it was made as packaging materials. Generally, antibacterial properties of

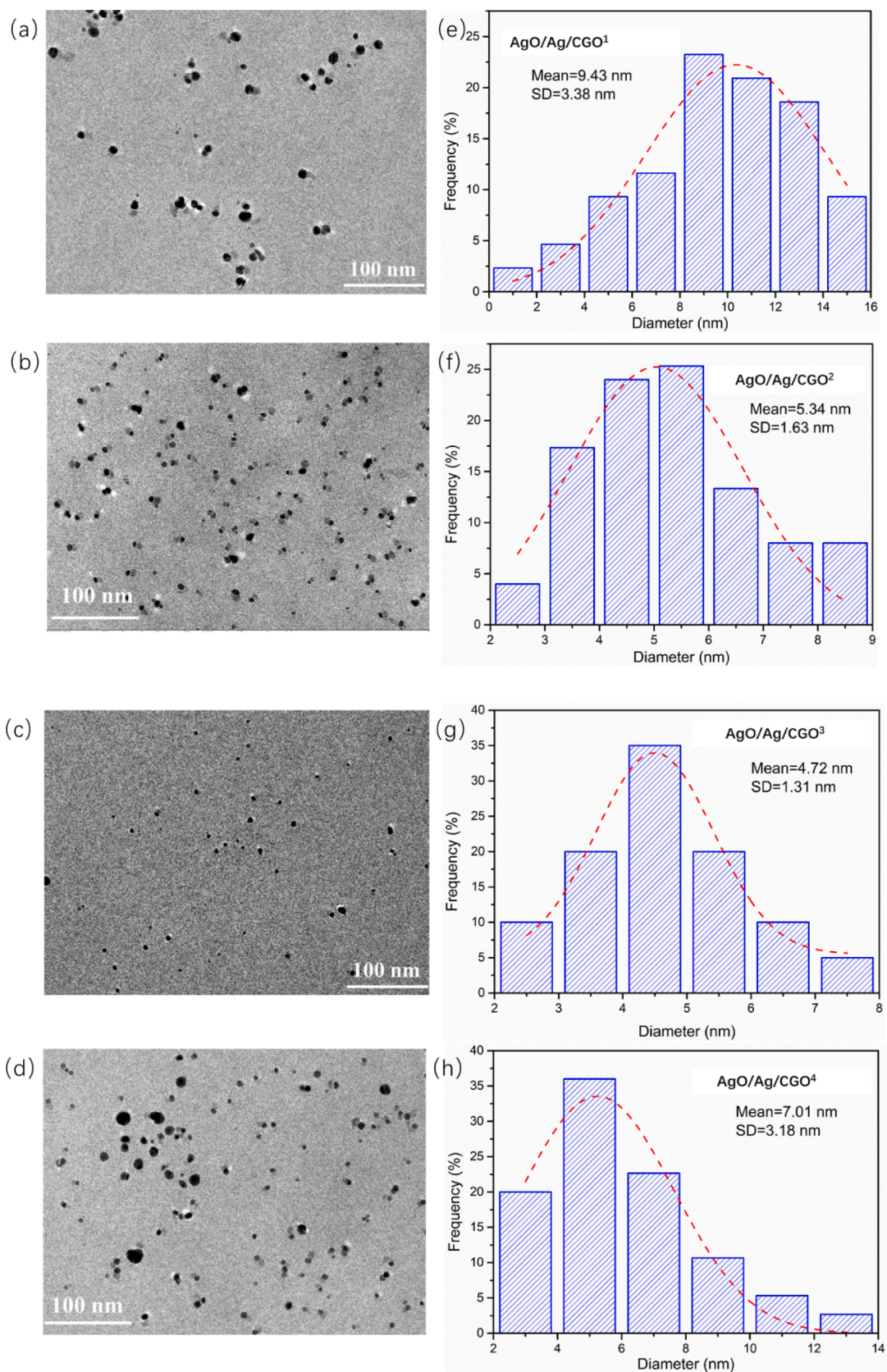


Fig. 6. TEM images and corresponding size distributions of fabricated AgO/Ag/CGO¹, AgO/Ag/CGO², AgO/Ag/CGO³ and AgO/Ag/CGO⁴.

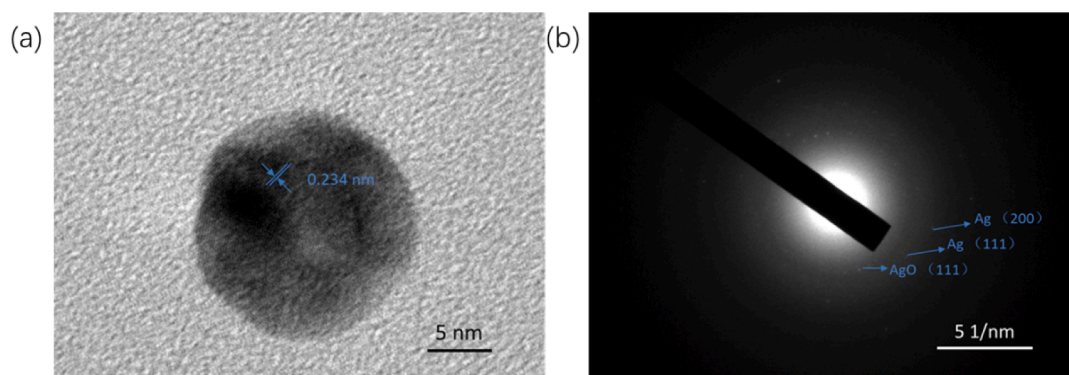


Fig. 7. HRTEM image and SADE pattern of AgO/Ag/CGO³.

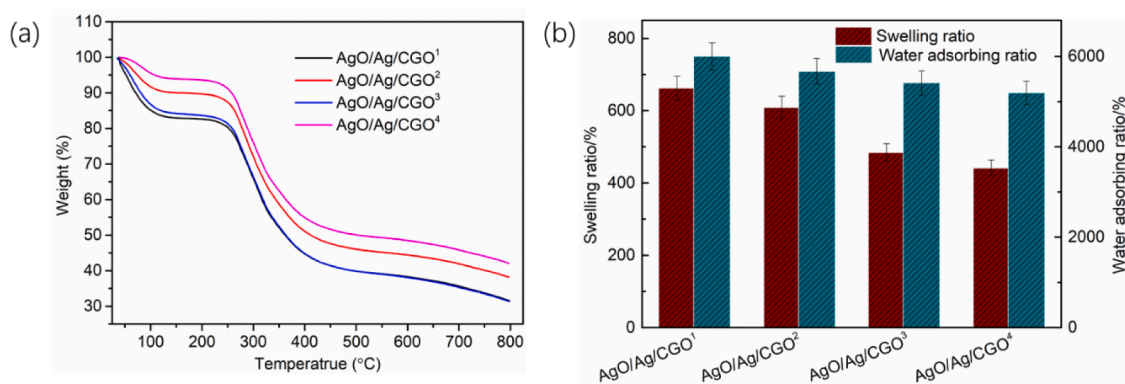


Fig. 8. (a) TGA curves and (b) Water adsorbing ratio in water and swelling behavior in PBS 7.4 of AgO/Ag/CGO¹, AgO/Ag/CGO², AgO/Ag/CGO³ and AgO/Ag/CGO⁴.

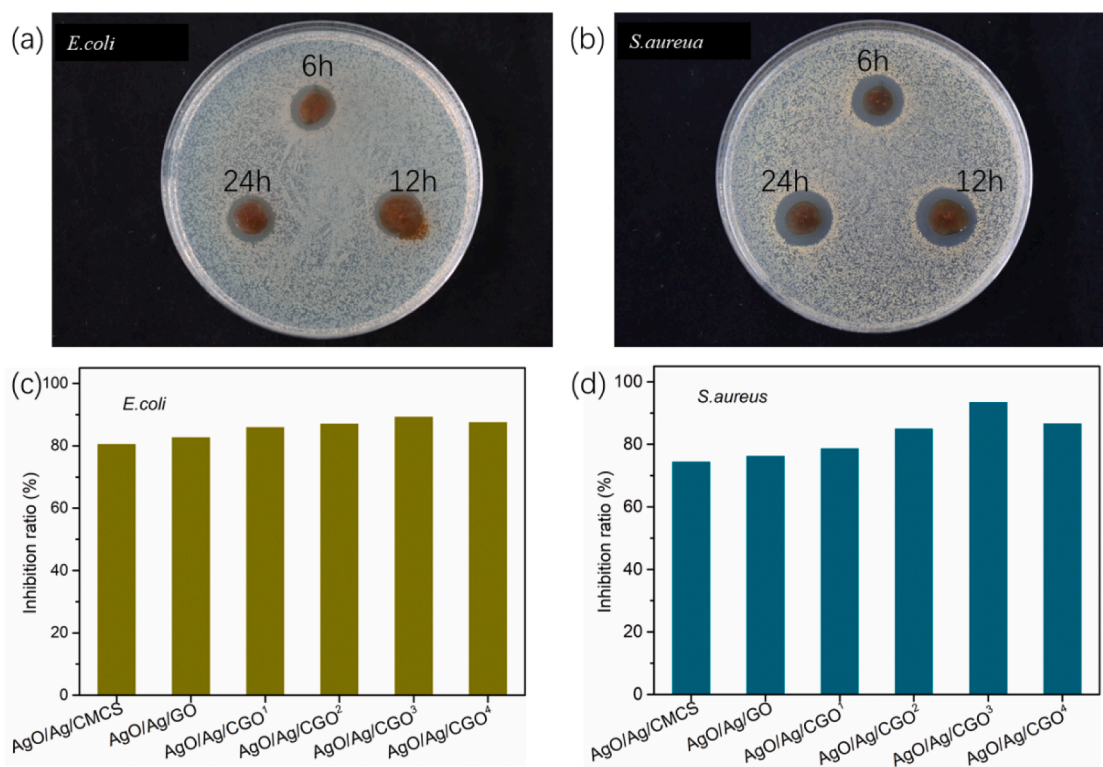


Fig. 9. Photograph of the inhibition zone of the AgO/Ag/CGO², AgO/Ag/CGO³ and AgO/Ag/CGO⁴ against (a) *E. coli* and (b) *S. aureus* and bacteriostatic rate of the films against (c) *E. coli* and (d) *S. aureus*.

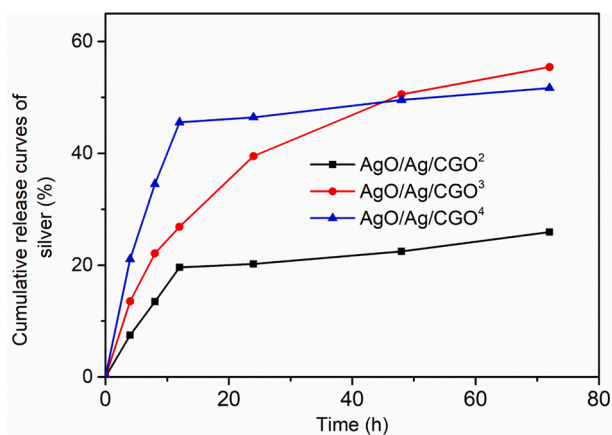


Fig. 10. In vitro silver release time profiles of AgO/Ag/CGO², AgO/Ag/CGO³, AgO/Ag/CGO⁴.

AgO/Ag nanoparticles may be described based on following mechanisms (Prabhu and Poulouse, 2012; Pandey and Ramontja, 2016): (1) AgO/Ag nanoparticles react with phosphorus and sulfur groups of bacterial DNA, which result in the disruption of DNA replication, (2) the Ag ions released from Ag nanoparticles penetrate into bacteria that lead to the disruption of DNA replication and ATP production by damaging the peptidoglycan, DNA, and protein (3) AgO/Ag nanoparticles attached to the surface of bacteria's membrane, which disturb its permeability and respiration ability during their interaction cell wall of bacteria. The cytotoxicity were evaluated using in vitro studies with a human pancreatic cancer cell line (HepG2) to evaluate the biosafety of the film. Biocompatibility is crucial for the film to be applied in the packing material. So we have tested the cytotoxicity of AgO/Ag/CGO³ on HepG2 cells via the MTT assay, and cell viability was determined after 24 h. The obtained results are presented in Fig. S2. It is obvious from the result, we can concluded that there is no significant change in the HepG2 cell after 24 h incubation with 1 to 10 $\mu\text{g mL}^{-1}$. In each concentration of the sample, over 90 % of the cells stayed alive, which suggests that the nanocomposite is not cytotoxic. And this antimicrobial AgO/Ag/CGO films can be applied in food packaging materials or controlled-release carrier material.

3.6. In vitro silver-release study

The in vitro release profiles of silver from the AgO/Ag/CGO², AgO/Ag/CGO³, AgO/Ag/CGO⁴ were assessed and the results are presented in Fig. 10. As shown in Fig. 10, AgO/Ag/CGO² exhibited an initial burst release followed by subsequent slower release. The release of silver reaches a maximum of 25.9 % in pH 7.4 PBS. The initial burst release of silver may be attributed to the rapid dissolution of free AgNPs suspended in the phosphate buffer, as well as the discrete AgNPs attached on the surface of CGO. The AgO/Ag/CGO³ showed stable and continuous silver release with no obvious initial burst. This is because that AgNPs were well dispersed in AgO/Ag/CGO³ and they firmly anchored and embedded inside the CGO-polymer network. In addition, the strong interactions between silver and CGO prevented the fast dissolution of AgNPs to silver ions and the diffusion of silver ions into phosphate buffer, allowing AgO/Ag/CGO³ to release silver in a controlled way. In sharp contrast, AgO/Ag/CGO⁴ showed very fast silver release in the early stage and the release rate slowed. The initial burst release may be due to the rapid dissolution of free AgNPs, which were suspended in the phosphate buffer or attached on the surface of CGO. In addition, gelatin molecules degrade into the small fragments under the long-term UV-irradiation source. When many gelatin molecules degrade into the small fragments at a high irradiation time, some Ag-NPs that cannot be enveloped in the gelatin framework agglomerate into larger particles on

the surface of CGO. Thus, the initial burst release was obvious. Therefore, AgO/Ag/CGO³ had much better performance in retaining silver for prolonged periods. Besides, in the case of AgO/Ag/CGO³ is not cytotoxic and has excellent antimicrobial. This may help expand its potential applications in food packaging materials or controlled-release carrier material.

4. Conclusion

In summary, antimicrobial AgO/Ag/CGO films were synthesized successfully by UV irradiation and ionic crosslinking method. Benefiting from the green and simple method, the Ag nanoparticles with a small size ($4.72 \pm 1.31 \text{ nm}$) was successfully synthesized, which will benefit to the antimicrobial of AgO/Ag/CGO films. Our study found that, the addition of GO improve the thermal stability and swelling ratio of AgO/Ag/CGO films. The results of cytotoxicity of AgO/Ag/CGO³ on HepG2 cells suggests that the nanocomposite is not cytotoxic, and the cell viabilities were still higher than 80 %. Furthermore, we concluded that the AgO/Ag/CGO³ exhibited better antimicrobial activity than AgO/Ag/CGO² and AgO/Ag/CGO⁴ from the result of bacteriostatic zone test and the inhibition rate test (*E. coli* 89.2 % and *S. aureus* 93.4 %). We also obtained that AgO/Ag/CGO³ exhibited stable and continuous silver release and better performance in retaining silver for prolonged periods owing to the strong coordination and electrostatic interactions between CGO and silver. Consequently, the simple and green method to prepare Ag-based antimicrobial films is promising and meaningful.

CRedit authorship contribution statement

Chen Li: Methodology, Investigation, Validation, Data curation, Writing – original draft. **Ke Wang:** Conceptualization. **Fayong Li:** Software. **Dong Xie:** Conceptualization, Supervision.

Declaration of competing interest

The authors declare that they have no known competing financial interests or personal relationships that could have appeared to influence the work reported in this paper.

Acknowledgements

This research was supported by the GDAS' Project of Science and Technology Development (nos. 2021GDASYL-20210103040); GDAS' Project of Science and Technology Development (nos. 2022GDASZH-2022010110); Guangzhou Science and Technology Project (nos. 202002030172).

Appendix A. Supplementary material

Supplementary data to this article can be found online at <https://doi.org/10.1016/j.arabjc.2023.105380>.

References

- Ali, H.U., Iqbal, D.N., Iqbal, M., Ezzine, S., Arshad, A., Zeeshan, R., Chaudhry, A.A., Alshawwa, S.Z., Nazir, A., Khan, A.F., 2022. HPMC crosslinked chitosan/hydroxyapatite scaffolds containing Lemongrass oil for potential bone tissue engineering applications. Arab. J. Chem., 103850
- Azeman, N.H., Bakar, M.H.A., Nazri, N.A.A., Mobarak, N.N., Khushaini, M.A.A., Aziz, T. H.T.A., MdZain, A.R., Bakar, A.A.A., 2022. Carboxymethyl chitosan/graphene oxide/silver nanotriangles nanohybrid as the sensing materials for the enhancement of ammonia localized surface plasmon resonance sensor. Opt. Laser Technol. 148, 107789.
- Baskar, K., Saravana Karthikeyan, B., Gurucharan, I., Mahalaxmi, S., Rajkumar, G., Dhivya, V., Kishen, A., 2022. Eggshell derived nano-hydroxyapatite incorporated carboxymethyl chitosan scaffold for dentine regeneration: a laboratory investigation. Int. Endod. J. 55, 89–102.
- Benucci, I., Liburdi, K., Cacciotti, I., Lombardelli, C., Zappino, M., Nanni, F., Esti, M., 2018. Chitosan/clay nanocomposite films as supports for enzyme immobilization:

- An innovative green approach for winemaking applications. *Food Hydrocolloid*. 74, 124–131.
- Biao, L., Tan, S., Wang, Y., Guo, X., Fu, Y., Xu, F., Zu, Y., Liu, Z., 2017. Synthesis, characterization and antibacterial study on the chitosan-functionalized Ag nanoparticles. *Mater. Sci. Eng. C* 76, 73–80.
- Biswas, S., Fatema, J., Debnath, T., Rashid, T.U., 2021. Chitosan–clay composites for wastewater treatment: a state-of-the-art review. *ACS EST Water* 1, 1055–1085.
- Cao, J., He, G., Ning, X., Chen, X., Fan, L., Yang, M., Yin, Y., Cai, W., 2022. Preparation and properties of O-chitosan quaternary ammonium salt/polyvinyl alcohol/graphene oxide dual self-healing hydrogel. *Carbohydr. Polym.*, 119318.
- Cheng, Y., Wei, Y., Fang, C., Li, H., Chen, J., Zhang, J., Huang, Z., 2021. Facile synthesis of chitosan/Ag-waterborne polyurethane composite films with a high stability and controllable water resistance for potential application in antibacterial materials. *J. Mater. Res. Technol.* 15, 5316–5325.
- Duan, C., Liu, C., Meng, X., Gao, K., Lu, W., Zhang, Y., Dai, L., Zhao, W., Xiong, C., Wang, W., Liu, Y., Ni, Y., 2020. Facile synthesis of Ag NPs@ MIL-100 (Fe)/guar gum hybrid hydrogel as a versatile photocatalyst for wastewater remediation: photocatalytic degradation, water/oil separation and bacterial inactivation. *Carbohydr. Polym.* 230, 115642.
- Eddarai, E.M., El Mouzahim, M., Boussem, R., Bellaouchou, A., Guenbour, A., Zarrouk, A., 2022. Chitosan-kaolinite clay composite as durable coating material for slow release NPK fertilizer. *Int. J. Biol. Macromol.* 195, 424–432.
- Furtos, G., Tomoaia-Cotisel, M., Garbo, C., Şenilă, M., Jumate, N., Vida-Simiti, I., Prejmerean, C., 2013. New composite bone cement based on hydroxyapatite and nanosilver. *Particul. Sci. Technol.* 31, 392–398.
- Gao, F., Mi, Y., Wu, X., Yao, J., Qi, Q., Chen, W., Cao, Z., 2022. Preparation of quaternized chitosan/Ag composite nanogels in inverse miniemulsions for durable and antimicrobial cotton fabrics. *Carbohydr. Polym.* 278, 118935.
- Gasti, T., Dixit, S., Hiremani, V.D., Chougale, R.B., Masti, S.P., Vootla, S.K., Mudigoudra, B.S., 2022. Chitosan/pullulan based films incorporated with clove essential oil loaded chitosan-ZnO hybrid nanoparticles for active food packaging. *Carbohydr. Polym.* 277, 118866.
- Gils, P.S., Ray, D., Sahoo, P.K., 2010. Designing of silver nanoparticles in gum arabic based semi-IPN hydrogel. *Int. J. Biol. Macromol.* 46, 237–244.
- Hao, Y., Zhao, W., Zhang, H., Zheng, W., Zhou, Q., 2022. Carboxymethyl chitosan-based hydrogels containing fibroblast growth factors for triggering diabetic wound healing. *Carbohydr. Polym.*, 119336.
- He, X., Gopinath, K., Sathishkumar, G., Guo, L., Zhang, K., Lu, Z., Li, C., Kang, E.T., Xu, L., 2021. UV-assisted deposition of antibacterial Ag–tannic acid nanocomposite coating. *ACS Appl. Mater. Interfaces* 17, 20708–20717.
- He, M., Lu, T., Jia, Z., Tian, H., Feng, M., Zhang, X., Zhang, M., Wang, C., Zhao, Y., Qiu, J., 2022. Fabrication and properties of novel chitosan/ZnO composite bioplastic. *Cellul.* 29, 233–243.
- Hosseini, S.F., Zandi, M., Rezaei, M., Farahmandghavi, F., 2013. Two-step method for encapsulation of oregano essential oil in chitosan nanoparticles: preparation, characterization and in vitro release study. *Carbohydr. Polym.* 95, 50–56.
- Huang, S., Yu, Z., Zhang, Y., Qi, C., Zhang, S., 2017. In situ green synthesis of antimicrobial carboxymethyl chitosan–nanosilver hybrids with controlled silver release. *Int. J. Nanomed.* 12, 3181.
- Jie, Y., Chen, F., Zhu, T., Lv, D., 2022. High internal phase emulsions stabilized solely by carboxymethyl chitosan. *Food Hydrocolloid*. 127, 107554.
- Kausar, A., Naeem, K., Hussain, T., Bhatti, H.N., Jubeen, F., Nazir, A., Iqbal, M., 2019. Preparation and characterization of chitosan/clay composite for direct Rose FRN dye removal from aqueous media: comparison of linear and non-linear regression methods. *J. Mater. Res. Technol.* 8, 1161–1174.
- Lashin, I., Fouda, A., Gobouri, A.A., Azab, E., Mohammedsah, Z.M., Makharita, R.R., 2021. Antimicrobial and in vitro cytotoxic efficacy of biogenic silver nanoparticles (Ag-NPs) fabricated by callus extract of *Solanum incanum* L. *Biomolecules* 11, 341.
- Lewandowska, K., Sionkowska, A., Kaczmarek, B., Furtos, G., 2014a. Characterization of chitosan composites with various clays. *Int. J. Biol. Macromol.* 65, 534–541.
- Lewandowska, K., Sionkowska, A., Kaczmarek, B., Furtos, G., 2014b. Mechanical and morphological studies of chitosan/clay composites. *Mol. Cryst. Liq. Cryst.* 590, 193–198.
- Luo, J., Fan, C., Xiao, Z., Sun, T., Zhou, X., 2019. Novel graphene oxide/carboxymethyl chitosan aerogels via vacuum-assisted self-assembly for heavy metal adsorption capacity. *Colloid. Surf. A* 578, 123584.
- Nguyen, T.H.N., Nguyen, T.D., Cao, M.T., 2020. Fast and simple synthesis of triangular silver nanoparticles under the assistance of light. *Colloid. Surf. A* 594, 124659.
- Niu, Z., Zhou, C., Wang, J., Xu, Y., Gu, C., Jiang, T., Zeng, S., Zhang, Y., Ang, D.S., Zhou, J., 2020. UV-light-assisted preparation of MoO_{3-x}/Ag NPs film and investigation on the SERS performance. *J. Mater. Sci.* 55, 8868–8880.
- Nwanya, A.C., Ugwuoke, P.E., Ezekoye, B.A., Osuji, R.U., Ezema, F.I., 2013. Structural and optical properties of chemical bath deposited silver oxide thin films: role of deposition time. *Adv. Mater. Sci. Eng.*, 450820.
- Olanipekun, E.O., Ayodele, O., Olatunde, O.C., Olusegun, S.J., 2021. Comparative studies of chitosan and carboxymethyl chitosan doped with nickel and copper: Characterization and antibacterial potential. *Int. J. Biol. Macromol.* 183, 1971–1977.
- Pan, J., Zhang, Z., Zhan, Z., Xiong, Y., Wang, Y., Cao, K., Chen, Y., 2020. In situ generation of silver nanoparticles and nanocomposite films based on electrodeposition of carboxylated chitosan. *Carbohydr. Polym.* 242, 116391.
- Pandey, S., Ramontja, J., 2016. Sodium alginate stabilized silver nanoparticles–silica nanohybrid and their antibacterial characteristics. *Int. J. Boil. Macromol.* 93, 712–723.
- Prabhu, S., Poulouse, E.K., 2012. Silver nanoparticles: mechanism of antimicrobial action, synthesis, medical applications, and toxicity effects. *Int. Nano Lett.* 2, 32.
- Rostamian, M., Hosseini, H., Fakhri, V., Talouki, P.Y., Farahani, M., Ghahreztzpeh, A.J., Goodarzi, V., Su, C.H., 2022. Introducing a bio sorbent for removal of methylene blue dye based on flexible poly (glycerol sebacate)/chitosan/graphene oxide ecofriendly nanocomposites. *Chemosphere* 289, 133219.
- Samsuddin, A.F., Aziz, S.N.Q.A.A., Pung, S.Y., 2017. Loading effect of Ag/AgO on the photocatalytic performance of ZnO rods. *Appl. Phys. A* 123, 1–12.
- Shariatnia, Z., 2018. Carboxymethyl chitosan: Properties and biomedical applications. *Int. J. Boil. Macromol.* 120, 1406–1419.
- Su, J., Jia, Y., Hou, R., Huang, Y., Shen, K., Hao, Z., 2021. Preparation and characterization of graphene oxide/O-carboxymethyl chitosan (GO/CMC) composite and its unsymmetrical dimethylhydrazine (UDMH) adsorption performance from wastewater. *Environ. Technol.* 1–12.
- Wardana, A.A., Kingwascharapong, P., Wigati, L.P., Tanaka, F., Tanaka, F., 2022. The antifungal effect against *Penicillium italicum* and characterization of fruit coating from chitosan/ZnO nanoparticle/Indonesian sandalwood essential oil composites. *Food Packaging Shelf* 32, 100849.
- Xu, Y., Liu, J., Guan, S., Dong, A., Cao, Y., 2020. A novel Ag/AgO/carboxymethyl chitosan bacteriostatic hydrogel for drug delivery. *Mater. Res. Express* 7, 085403.
- Zhang, M., Yang, M., Woo, M.W., Li, Y., Han, W., Dang, X., 2021. High-mechanical strength carboxymethyl chitosan-based hydrogel film for antibacterial wound dressing. *Carbohydr. Polym.* 256, 117590.
- Zhou, P., Xia, Z., Qi, C., He, M., Yu, T., Shi, L., 2021. Construction of chitosan/Ag nanocomposite sponges and their properties. *Int. J. Biol. Macromol.* 192, 272–277.